THE JOURNAL OF PHYSICAL CHEMISTRY C
A JOURNAL OF THE AMERICAN CHEMICAL SOCIETY

pubs.acs.org/JPCC

Article

ReaxFF Study of Surface Chemical Reactions between α-Al_2O_3 Substrates and H_2O/H_2 Gas-Phase Molecules

Yuwei Zhang, Nadire Nayir, Yun Kyung Shin, Qian Mao, Ga-Un Jeong, Chen Chen, Joan M. Redwing, and Adri C. T. van Duin*

Cite This: *J. Phys. Chem. C* 2024, 128, 18767−18781

Read Online

ACCESS | Metrics & More | Article Recommendations | Supporting Information

ABSTRACT: We developed an Al/O/H ReaxFF force field to explore chemical reactions on α-Al_2O_3 surfaces in H_2O/H_2 gas-phase environments. This force field generates surface energy profiles of A-, C-, R-, and M-planes with various terminations (Al- or O-) and predicts the thermodynamic and kinetic behaviors of hydrolysis on Al-terminated α-Al_2O_3 (0001), consistent with quantum chemical studies. Molecular dynamics (MD) simulations of H_2O/α-Al_2O_3 (0001) reveal that water autocatalysis plays a significant role in accelerating H_2O dissociations on Al-terminated α-Al_2O_3 (0001). Compared with the 50% Al-terminated surface, the 100% Al-terminated surface becomes more easily hydroxylated at temperatures as low as 350 K, relying more on an O_xH_y clustering mechanism than complete H_2O dissociations, and desorbs significantly more H_2O molecules once heated up to 500 K or higher. But heating cannot eliminate surface hydroxyls for either case, and achieving a Gibbsite-like surface by H_2O exposure is unlikely. H_2O dissociations on α-Al_2O_3 (0001) terminated with randomly distributed surface Al species deviate from 1−2 and 1−4 pathways due to irregular vacancy defects, and a random surface appears to be more reactive to H_2O than the ordered one with the same surface Al coverage. Simulations of H_2/α-Al_2O_3 suggest that the combination of a dense surface O coverage and a low thermodynamic surface stability leads to elevated H_2 dissociation kinetics. To accelerate the surface O removals of 100% O-terminated α-Al_2O_3 (0001) in H_2 gas exposure, we reduced the H−H σ bond energy parameter, equivalent to lowering the H_2 dissociation barrier by ∼ 19.4 kcal/mol during the simulation. After ∼ 1.5 ns, the surface termination became comparable to the 100% Al-terminated one but retained a small quantity of hydroxyls. This force field reveals how the α-Al_2O_3 crystallographic plane and the surface termination influence the dissociation behaviors of H_2O/H_2 gas molecules and lays the foundation for future force field developments targeted at thin film epitaxy on sapphire.

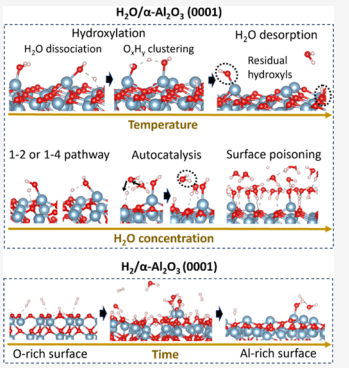

1. INTRODUCTION

Surface chemistry and geometry play pivotal roles in determining the epitaxial behavior of thin films, ultimately shaping their solid-state properties. Numerous strategies have been proposed to manipulate the morphology of as-grown thin films, as discussed in recent literature reviews.[1,2] Of particular focus are studies exploring the impact of substrate surface properties such as hydrophobicity/hydrophilicity, polarity, and nanoscale topology on thin film morphology.[3−7] Substrate surface engineering has become an effective means to modulate and control the nucleation and growth behavior, which is particularly important for ultrathin film two-dimensional (2D) materials. For example, Zhu et al.[8] demonstrated that the surface oxygen elimination and the homogeneous Se passivation of sapphire substrates improved the unidirectional lattice alignment of WSe_2 flakes. Pradhan et al.[9] reported that an H_2 ambient released the interfacial stress and diminished the interfacial defects during the MoS_2 epitaxy on silicon, suppressing the out-of-plane growth of MoS_2. Najmaei et al.[10] created step edges on the substrate using conventional lithography to guide the formation of MoS_2 triangular domains and significantly reduced the grain boundaries in the centimeter-sized as-grown MoS_2 monolayers.

α-aluminum oxide (α-Al_2O_3) is the most stable crystalline form among polymorphs of alumina.[11] It has the space group $R\bar{3}c$, where Al^{3+} cations occupy two-thirds of the octahedral sites of the slightly distorted hexagonal close-packed skeleton constructed by O^{2-} anions. The α-Al_2O_3 has been widely utilized in electronic devices and manufacturing and employed as substrates for thin film growth.[12−17] Recent breakthroughs in the epitaxial growth of wafer-scale transition-metal dichalcogenides (TMDs) suggest that crystalline sapphire is one of the most promising substrates to grow large-scale single-crystal TMD nanosheets.[8,18−25] The α-Al_2O_3 has similar crystallographic symmetry and commensurable lattice constants with TMDs, so it can trigger preferred lattice

Received: July 11, 2024
Revised: October 15, 2024
Accepted: October 16, 2024
Published: October 29, 2024

orientations during TMD epitaxy and induce seamless merging of the as-grown flakes without introducing grain boundaries. However, reproducing large-scale single-crystal TMD nanosheets relies on many factors.[23,24,26−28] Understanding these factors is crucial for optimizing the synthesis of high-quality TMD monolayers. As the scientific community becomes more aware of the complex reactions occurring on the sapphire surface and their relevance to the epitaxial growth of TMD monolayers, there is a growing interest in computational studies to guide the synthesis of 2D materials, enabling atomic-level insights into wafer-size epitaxial TMD growth mechanisms.[29,30] The TMD growth mechanisms are significantly influenced by the substrate surface compositions and morphologies. In the epitaxial growth of TMD monolayers by MOCVD, the sapphire substrate is typically preannealed in H_2 or air at high temperatures (~900 °C) before the growth. This preannealing process is known to alter the sapphire surface chemistry, resulting in the variation of OH- vs Al-terminated α-Al_2O_3 surface, which will affect the subsequent TMD nucleation through quasi-van der Waals epitaxy mechanisms. Additionally, sapphire surface steps decompose and agglomerate, giving rise to significant surface reorganization. This reorganization changes the sapphire's step height and leads to the terrace reconstruction, which will affect the domain alignment and epitaxial properties.[8] By introducing proper surface engineering with atomic-level details, we can enhance TMD epitaxy and reproducibly achieve wafer-scale single-crystal monolayers on sapphire substrates.[8,26,31,32]

The surface property of α-Al_2O_3 has been a popular topic and attracted numerous theoretical investigations because of its important role in thin film growth.[33,34] Sun et al.[35] performed Hartree−Fock calculations on the surface structures and energies for stoichiometric α-Al_2O_3 along five different crystallographic planes and reported the energy trend of the relaxed surfaces as $(0001) < (10\bar{1}2) < (11\bar{2}0) < (10\bar{1}0) < (10\bar{1}1)$. Kurita et al.[36] applied density functional theory (DFT) to calculate variously terminated C-, A-, and R-planes of α-Al_2O_3 with different stoichiometries. They reported the surface energy trend of stoichiometric α-Al_2O_3 as C < R < A, i.e., $(0001) < (1\bar{1}02) < (11\bar{2}0)$, and generated the surface energy profiles of nonstoichiometric α-Al_2O_3 subjected to the change of local chemical environments. Hütner et al.[37] applied DFT calculations on α-Al_2O_3 (0001) models prepared using atomic positions sourced from experimental data as well as machine learning optimization and realized the $(\sqrt{31} \times \sqrt{31})$ R ± 9° surface reconstruction with subsurface O species protruding the top layer Al. Their work reveals that the undercoordinated surface Al species relax inward to increase the coordination, leading to an in-plane expansion at the surface, which results in a $(\sqrt{31} \times \sqrt{31})$ R ± 9° reconstruction for fitting the expanded surface onto the corundum bulk structure. Interactions between α-Al_2O_3 and H_2/H_2O molecules have been widely studied experimentally and theoretically.[38,39] Particularly, the surface hydroxylation and the gas molecule desorption at different temperatures and surface terminations have been of great interest. A recent study done by Ranea et al.[40] reveals the mechanisms of hydrolysis on α-Al_2O_3(0001) at the DFT level. They reported two distinct H_2O dissociation pathways, namely, 1−2 and 1−4 pathways, and compared H_2O dissociations at dry, monohydroxylated, and dihydroxylated Al-O sites, suggesting that a Gibbsite-like surface may not be obtained by simple H_2O dissociations. In another work, Wang et al.[41] discovered that even though the 1−2 H_2O dissociation is more thermodynamically favored than the 1−4 pathway, the latter is more kinetically favored at low temperatures due to a lower energy barrier than the former. Also, the in-plane diffusion of protons results in the isomerization between 1−2 and 1−4 hydroxylated products on α-Al_2O_3(0001). Yue et al.[42] reported that neither the H_2O chemisorption on an Al-terminated α-Al_2O_3(0001) surface nor the H_2O desorption on a Gibbsite-like surface can interconvert the two surface terminations. The interest in probing H_2O molecular orientations and the structure of H_2O layers on sapphire has also emerged. Boily et al.[43] and Zhang et al.[44] explored the hydrogen bonding and H_2O orientations by sum-frequency generation spectroscopy and ab initio molecular dynamics (AIMD) simulations, respectively.

Despite the significant theoretical efforts on exploring α-Al_2O_3/H_2O interactions mentioned above, investigations that can temporally monitor the α-Al_2O_3 surface reactions in H_2/H_2O gas-phase environments beyond the quantum chemical (QC) length scale are still lacking. To bridge the gap between the first-principles predictions and the goal of guiding thin film epitaxy through computational methods, we developed a ReaxFF reactive force field to enable large-scale modeling of α-Al_2O_3 surface reaction dynamics at an accuracy close to that of QC methods. This Al/O/H force field was trained extensively against QC data, including surface energies of differently terminated A-, C-, R-, and M-planes of flat α-Al_2O_3 models. Additionally, we adopted DFT data of step-terrace models during the training in preparation for future research on modeling thin film growth guided by step edges. The hydrolysis process on α-Al_2O_3 was considered as well for accurately describing the H_2O dissociation behavior both thermodynamically and kinetically.

It is noteworthy that we will seek to expand this Al/O/H force field to include TMD elements such as W/Mo/S/Se by combining previous ReaxFF force fields,[45−48] which we believe will lay a good foundation for simulating complex surface reactions and revealing growth mechanisms of TMD epitaxy in future work.

2. REAXFF FORCE FIELD

The ReaxFF reactive force field, unlike traditional nonreactive force fields, is a bond-order-dependent interatomic potential capable of describing bond breaking and formation throughout simulations.[49] The bond order changes exponentially with the interatomic distance and determines the system energy; the interaction energy decreases to zero as the bond order approaches zero. In this way, systems can avoid abrupt energy changes during bond formations and bond breakages, which makes ReaxFF an ideal force field to describe complex chemical reactions. ReaxFF has been widely applied to explore interactive material systems, including but not limited to hydrocarbon combustions, heterogeneous catalysis, novel properties of 2D materials, and tribological behavior at material interfaces, etc.[50−53]

ReaxFF calculates the total energy of a system by summing up partial terms contributed by bonded and nonbonded interactions:

$$E_{system} = E_{bond} + E_{angle} + E_{tor} + E_{over} + E_{Coulomb} + E_{vdWaals} + E_{specific} \quad (1)$$

https://doi.org/10.1021/acs.jpcc.4c04669
J. Phys. Chem. C 2024, 128, 18767−18781

Energy contributions from covalent bonds E_{bond}, valence angles E_{angle}, torsion angles E_{tor}, and overcoordination penalties E_{over} are calculated with bond orders. Energy contributions from Coulomb $E_{Coulomb}$ and van der Waals $E_{vdWaals}$ interactions are nonbonded and are calculated between all atom pairs regardless of the connectivity. $E_{Coulomb}$ and $E_{vdWaals}$ are shielded to prevent excessive repulsions and attractions at short distances and are truncated smoothly by a distance-dependent Taper function at the cutoff distance.[54] $E_{specific}$ refers to specific cases not considered generally, such as lone pairs, hydrogen bonds, corrections for C_2, under-coordination corrections, etc.

The bond-order formula includes different bond types as its fractional terms:

$$BO'_{ij} = BO^{\sigma}_{ij} + BO^{\pi}_{ij} + BO^{\pi\pi}_{ij} \quad (2a)$$

$$= \exp\left[p_{bo,1}\left(\frac{r_{ij}}{r_0^{\sigma}}\right)^{p_{bo,2}}\right] + \exp\left[p_{bo,3}\left(\frac{r_{ij}}{r_0^{\pi}}\right)^{p_{bo,4}}\right] + \exp\left[p_{bo,5}\left(\frac{r_{ij}}{r_0^{\pi\pi}}\right)^{p_{bo,6}}\right] \quad (2b)$$

where the first, the second, and the third terms are contributed by sigma, pi, and double pi bonds, respectively. The equilibrium distances r_0^{σ}, r_0^{π}, $r_0^{\pi\pi}$ and the bonding parameters $p_{bo,1}$, $p_{bo,2}$, $p_{bo,3}$, $p_{bo,4}$, $p_{bo,5}$, and $p_{bo,6}$ are optimized during force field training procedures. Based on the deviation between the bond-order summation from all the neighboring atoms and the actual valence of a specific atom, corrected bond orders for all atom pairs are calculated, and so is the corrected over-coordination penalty for each atom.[55] E_{bond} is a function of the corrected bond orders. E_{angle} and E_{tor} are functions of the corrected bond orders and the corrected overcoordination penalties.

3. FORCE FIELD PARAMETERIZATION

3.1. Sources of Training Data. The force field parameters are system-dependent and need to be optimized against QC and/or experimental data with an algorithm using single-parameter parabolic search.[56] In this study, the initial training data taken from ref 45 includes DFT data of the formation energy and the volume/energy equations of state of bulk α-Al_2O_3. We expanded this data set by incorporating surface energies of stoichiometric and nonstoichiometric α-Al_2O_3 slabs, which are differently terminated along A-, C, M- and R-planes, as reported in refs 35,36. The initial parameters for the Al-atom, Al−Al and Al−O bonds, Al−O off-diagonal, and Al−O-related angle parameters were adopted from ref 45. Then, we retrained these parameters against DFT data of the hydroxylation and the hydrogen diffusion energies of α-Al_2O_3 (0001) as well as the dehydration energy of fully hydroxylated terrace-step α-Al_2O_3 (0001),[8,40,41,57,58] specifically focusing on Al−O, Al−H, and Al−O−H-related parameters.

3.2. Properties of Bulk α-Al_2O_3. Table 1 presents the comparison of lattice parameters and the heat of formation for bulk α-Al_2O_3 at DFT, experiment, and ReaxFF levels, indicating that ReaxFF values are in good agreement with those predicted by DFT and experiments. The heat of formation is defined as $\Delta H_{Al_2O_3} = \mu_{Al_2O_3} - (3\ \mu_{O(gas)} + 2\ \mu_{Al(bulk\text{-}fcc)})$, where $\mu_{Al_2O_3}$ is the total energy of an Al_2O_3 unit in bulk α-Al_2O_3. $\mu_{O(gas)}$ and $\mu_{Al(bulk\text{-}fcc)}$ are chemical potentials of the O and Al atoms referenced to the O_2 molecule and the Al(fcc) lattice. Figure 1 shows the equations of state of bulk α-Al_2O_3 under a sequence of volume changes from compressed to expanded states.

Table 1. Lattice Parameters and the Heat of Formation (ΔH) of Bulk α-Al_2O_3 Obtained from DFT, Experiments, and ReaxFF

	Axial lengths (Å) $a = b = c$	Axial angles (deg) $\alpha = \beta = \gamma \neq 90°$	Heat of formation ΔH (kcal/mol)
DFT[36]	5.17	55.43°	−352.83
Experiment[36]	5.128	55.33°	−396.65
ReaxFF	5.178	55.29°	−396.01

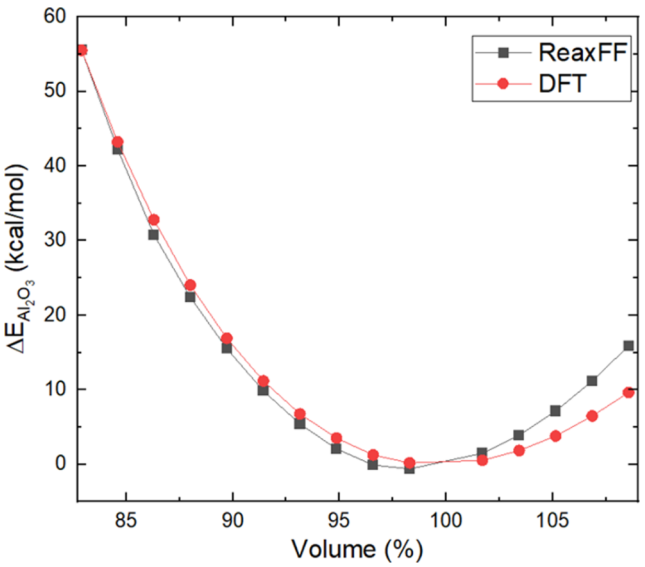

Figure 1. Equations of state of bulk α-Al_2O_3 calculated by DFT[59,60] and ReaxFF.

3.3. Surface Energies of Flat α-Al_2O_3 Models. Figure S1 illustrates the geometry of variously terminated crystallographic planes (A-, C-, R-, and M-) utilized in force field training. The surface labels correspond to those in Table 2.

Table 2. Flat α-Al_2O_3 Models Were Used to Train Surface Energies; Surface Names of the Stoichiometric Models Are Written with Bold Letters

Surface name	Crystallographic plane	Surface termination	Stoichiometry
A_Al_I	A $(11\bar{2}0)$	100% surface Al	non-
A_O_I	A $(11\bar{2}0)$	50% surface O	stoichiometric
A_O_II	A $(11\bar{2}0)$	33.3% surface O	non-
A_O_III	A $(11\bar{2}0)$	100% surface O	non-
A_O_IV	A $(11\bar{2}0)$	66.7% surface O	non-
C_Al_I	C (0001)	50% surface Al	stoichiometric
C_Al_II	C (0001)	100% surface Al	non-
C_O_I	C (0001)	100% surface O	non-
M_Al	M $(10\bar{1}0)$	100% surface Al	stoichiometric
R_Al_I	R $(1\bar{1}02)$	Al (type I)	non-
R_Al_II	R $(1\bar{1}02)$	Al (type II)	non-
R_O_I	R $(1\bar{1}02)$	O (type I)	stoichiometric
R_O_II	R $(1\bar{1}02)$	O (type II)	non-
R_O_III	R $(1\bar{1}02)$	O (type III)	non-

https://doi.org/10.1021/acs.jpcc.4c04669
J. Phys. Chem. C 2024, 128, 18767−18781

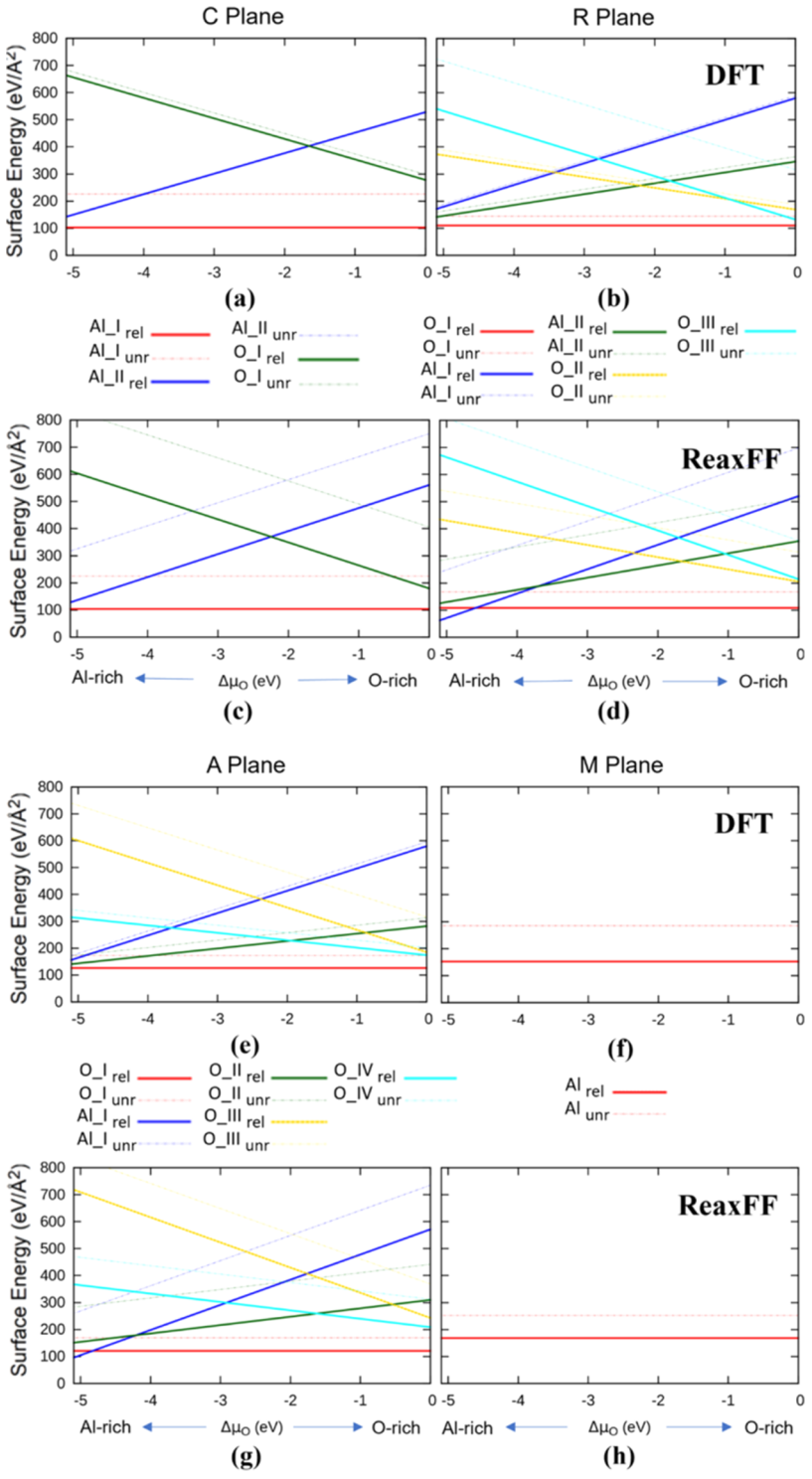

Figure 2. Surface energies of flat α-Al_2O_3 models. Panels (a), (b), (e), and (f) plot the DFT calculated surface energies of C, R, A, and M-planes, respectively.[35,36] Panels (c), (d), (g), and (h) plot the ReaxFF calculated surface energies of C, R, A, and M-planes, respectively. The symbols Al_I in panel (a), O_I in panel (b), O_I in panel (e), and Al in panel (f) denote the stoichiometric C, R, A, and M-planes, respectively; the rest of the symbols in the legends represent nonstoichiometric slabs. The subscripts "rel" and "unr" refer to the relaxed surface and the unrelaxed surface, respectively.

Cleaving a bulk material along a low-index crystallographic plane results in a slab that either maintains the identical stoichiometry with the bulk or exhibits nonstoichiometry at the termination. The surface energy of a stoichiometric α-Al_2O_3 slab is defined as $E_{surface} = E_{slab} - n_{Al_2O_3} \times \mu_{Al_2O_3}$, which is directly calculable from $\mu_{O(gas\text{-}phase)}$, $\mu_{Al(bulk\text{-}fcc)}$, and $\Delta H_{Al_2O_3}$. On the other hand, slabs with nonstoichiometric terminations have excess surface Al or O species with chemical potentials μ_{Al} or μ_O, respectively, which are varied with the local chemical environment. The upper limit of μ_O is associated with the O-rich condition and is defined as the chemical potential of an O atom in the O_2 gas phase (i.e., $\mu_{O(O\text{-}rich)} = \mu_{O(gas\text{-}phase)}$). The

https://doi.org/10.1021/acs.jpcc.4c04669
J. Phys. Chem. C 2024, 128, 18767−18781

lower limit of μ_O is calculated as $(\mu_{Al2O3} - 2\ \mu_{Al(bulk\text{-}fcc)})/3$, where $\mu_{Al(bulk\text{-}fcc)}$ is the upper limit of μ_{Al} or the chemical potential of an Al-atom in the FCC metal phase, since $\mu_{Al_2O_3} = 3\ \mu_O + 2\ \mu_{Al}$ is always satisfied.

$$(\mu_{Al_2O_3} - 2\mu_{Al(bulk\text{-}fcc)})/3 < \mu_O < \mu_{O(O\text{-}rich)} \quad (3)$$

$$(\mu_{Al_2O_3} - 2\mu_{Al(bulk\text{-}fcc)})/3 - \mu_{O(gas\text{-}phase)} < \mu_O - \mu_{O(O\text{-}rich)} < 0 \quad (4)$$

In other words, the surface energy of a nonstoichiometric slab $E_{surface} = E_{slab} - (n_{Al} \times \mu_{Al} + n_O \times \mu_O)$ is a linear function of μ_O or the excess O-chemical potential $\Delta\mu_O = \mu_O - \mu_{O(O\text{-}rich)}$ ranging in (5). So, the surface energies obtained at the upper and the lower limits of μ_O completely define the surface energy profile of a nonstoichiometric slab under the chemical environment ranging from the O-rich to the metal-rich conditions.

$$(\mu_{Al_2O_3} - 2\mu_{Al(bulk\text{-}fcc)})/3 - \mu_{O(gas\text{-}phase)} < \Delta\mu_O < 0 \quad (5)$$

The training results for all of the flat α-Al_2O_3 models are visualized in Figure S1b–e and are presented in Figure 2. $\Delta\mu_O$ has the maximum excess as 5.1 eV.[36] Compared to the DFT calculations, ReaxFF has successfully reproduced the relative thermodynamic stability of the stoichiometric slabs, indicating that the C-plane is the most stable surface, followed by the R-plane and then the A-plane. The M-plane is identified as the least stable configuration. Figure 2 also reproduces the energy profiles of relaxed surfaces for nonstoichiometric slabs, indicating that the thermodynamic stability of such surfaces depends on the local chemical environment. Irrespective of crystallographic planes, O-terminated surfaces tend to favor the O-rich condition and stabilize accordingly, whereas Al-terminated surfaces thermodynamically prefer the metal-rich condition.

3.4. Hydroxylation Energies of Flat α-Al_2O_3 (0001).

Hydroxylation energies and energy barriers through 1−2 and 1−4 H_2O dissociations on 50% Al-terminated α-Al_2O_3 (0001) were trained against DFT data reported in ref 40 and 41. Table S1 compares the DFT and ReaxFF values. Figure 3a shows the energy profiles of 1−2 and 1−4 H_2O dissociations on C_Al_I. In this figure, the O−H bond length between the dissociating O and H atoms is given together with the corresponding geometries in adsorption states, primary energy barriers, metastable states, secondary energy barriers, and dissociation states.

3.5. Dehydration Energies of Step-Terrace α-Al_2O_3 (0001).

Dehydration energies of fully hydroxylated α-Al_2O_3 (0001) step-terrace models (Figure 4) were trained against DFT data for both the H_2O-rich and the O-rich environments reported in ref8. The comparison of ReaxFF and DFT dehydration energies is presented in Figure S2. The removal of a surface O atom from a hydroxylated step-terrace α-Al_2O_3 (0001) surface in the form of H_2O exhibits distinct desorption behavior, depending on the thermodynamic stability of the desorption site. For example, the release of H_2O from the top terrace next to a step edge (1.179 eV in H_2O-rich and 4.156 eV in O-rich) is more energetically favored than those from the bottom terrace next to the step edge (1.797 eV in H_2O-rich and 4.773 eV in O-rich). This suggests that H_2O released from a hydroxylated step-terrace α-Al_2O_3 (0001) surface is not uniform; instead, it predominantly occurs at the top terrace

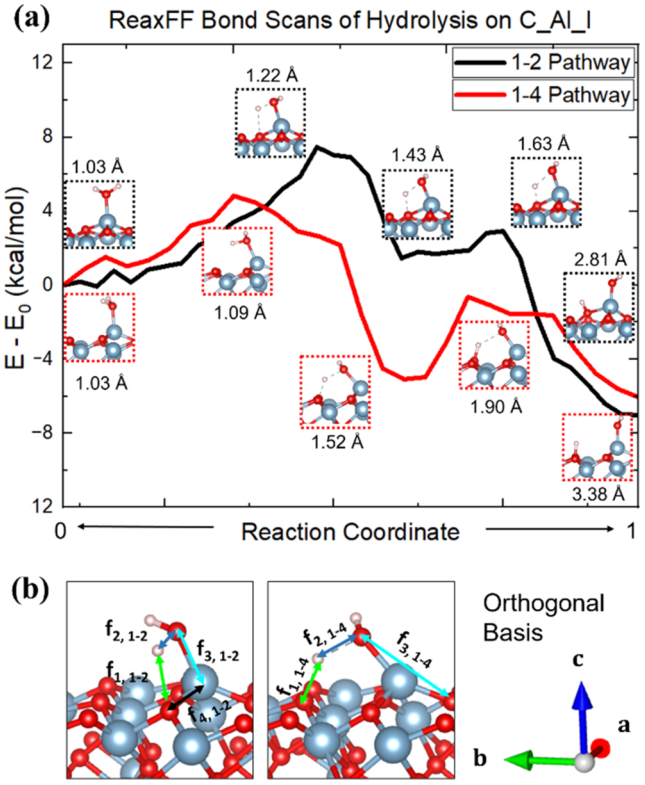

Figure 3. (a) Energy profiles of hydrolysis on 50% Al-terminated α-Al_2O_3 (0001) through 1−2 and 1−4 pathways. (b) Artificial forces applied to control interatomic distances during the bond scans. Primary force constants for generating artificial interatomic forces introduced to the system are as follows: $f_{1,1-2}$ = 100 kcal/mol, $f_{2,1-2}$ = 10 kcal/mol, $f_{3,1-2}$ = 100 kcal/mol, $f_{4,1-2}$ = 100 kcal/mol, $f_{1,1-4}$ = 135 kcal/mol, and $f_{2,1-4}$ = 10 kcal/mol, $f_{3,1-4}$ = 35 kcal/mol. Al species are indicated with blue, O species are red, and H species are white.

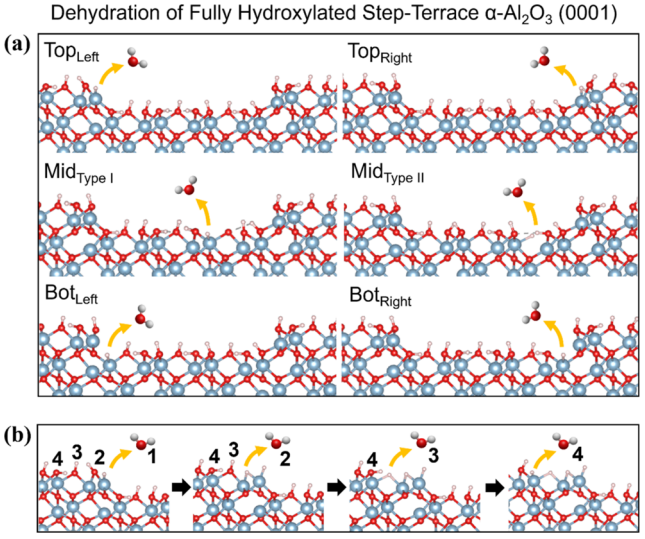

Figure 4. (a) Dehydration at the top left (Top_{Left}), top right (Top_{Right}), middle ($Mid_{Type\ I}$, $Mid_{Type\ II}$), bottom left (Bot_{Left}), and bottom right (Bot_{Right}) areas of the surface step. $Mid_{Type\ I}$ and $Mid_{Type\ II}$ represent O removals at two equivalent sites according to $R\bar{3}c$ symmetry. (b) Example of successive dehydrations starting from the top left area of the surface step.[8]

https://doi.org/10.1021/acs.jpcc.4c04669
J. Phys. Chem. C 2024, 128, 18767−18781

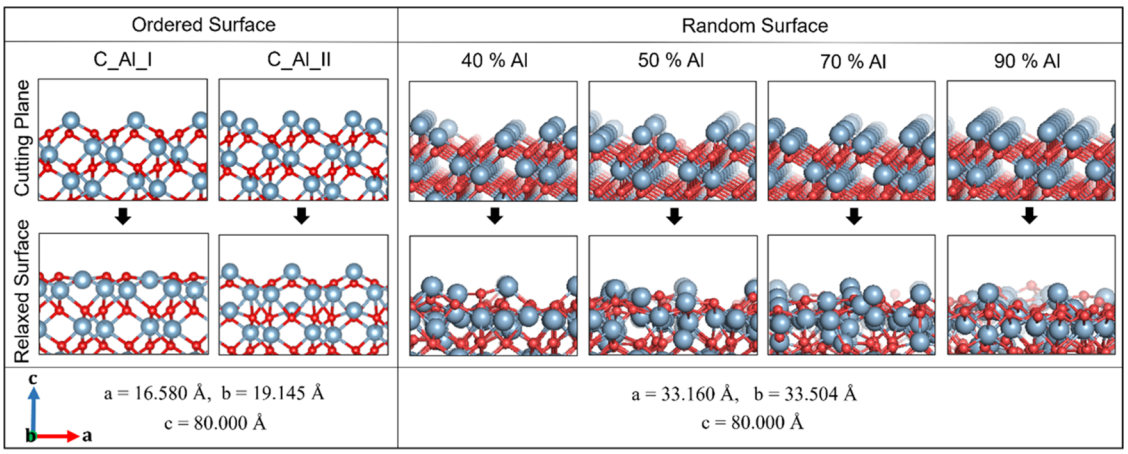

Figure 5. Flat α-Al_2O_3 (0001) models were used to study H_2O/α-Al_2O_3 (0001) interactions. Parameters a, b, and c are the dimensions of orthogonal simulation boxes.

next to the step edge. The bottom terrace exhibits less propensity to release H_2O, potentially leaving O impurities on an Al-terminated step-terrace surface, as corroborated by experiments in ref 8.

4. MD SIMULATION SETTINGS

4.1. H_2O/α-Al_2O_3 (0001) Interactions. To study H_2O/α-Al_2O_3 (0001) interactions, we constructed several individual samples consisting of an α-Al_2O_3 (0001) substrate and gas-phase H_2O molecules at different concentrations. These samples were relaxed at 300 K in an NPT ensemble using the Berendsen thermostat and barostat and then heated up (0.01 K/fs) to the temperatures of 350, 500, 700, 900, 1100, 1300, and 1500 K in an NVT ensemble using the Berendsen thermostat, and finally equilibrated at the target temperatures in the NVT ensemble for 0.5 ns. The parameters of the orthogonal simulation box and side views of α-Al_2O_3 (0001) substrates are presented in Figure 5. C_Al_I and C_Al_II refer to 50 and 100% Al-terminated α-Al_2O_3 (0001), respectively, which have ordered distributions of surface Al species. 40% Al, 50% Al, 70% Al, and 90% refer to 40, 50, 70, and 90% Al-terminated α-Al_2O_3 (0001) with randomly distributed surface Al species, respectively. The initial settings for H_2O/α-Al_2O_3 (0001) systems with different numbers of H_2O molecules are presented in Table 3 (ordered surfaces) and Table 4 (random surfaces). The ordered surfaces underwent reactions with 16, 32, 48, 64, 80, and 96 H_2O molecules; each system was kept at the target temperatures for 0.5 ns. The random surfaces underwent reactions with 112 H_2O molecules and were held isothermally at 700 K for 0.5 ns. The statistical analysis of H_2O chemisorption rates and O_xH_y clustering rates of ordered surfaces were averaged over 3 samples. The time step size used for all cases was 0.15 fs. In the calculations of H_2O/α-Al_2O_3 (0001) interactions, mixed Berendsen thermostats were utilized. The α-Al_2O_3 (0001) substrate was heated with a temperature damping parameter as 100 fs, while the gas-phase molecules of H_2O were subjected to a weaker thermostat with a temperature damping parameter as 10^3 fs to avoid gas-phase clustering in the vacuum and remove the excess energy from gas/solid surface reactions, thus mimicking a high-vacuum environment.

Table 3. H_2O/α-Al_2O_3 Interactive Systems with Ordered α-Al_2O_3 (0001) Surfaces

System type	Initial H_2O number	H_2O/surface Al (C_Al_I)	H_2O/surface Al (C_Al_II)
16_H_2O	16	0.5 H_2O/Al	0.25 H_2O/Al
32_H_2O	32	1 H_2O/Al	0.5 H_2O/Al
48_H_2O	48	1.5 H_2O/Al	0.75 H_2O/Al
64_H_2O	64	2 H_2O/Al	1 H_2O/Al
80_H_2O	80	2.5 H_2O/Al	1.25 H_2O/Al
96_H_2O	96	3 H_2O/Al	1.5 H_2O/Al

Table 4. H_2O/α-Al_2O_3 Interactive Systems with Random α-Al_2O_3 (0001) Surfaces

Surface name	Initial H_2O number	H_2O/surface Al (random)
40% Al	112	1.25 H_2O/Al
50% Al	112	1 H_2O/Al
70% Al	112	0.71 H_2O/Al
90% Al	112	0.56 H_2O/Al

4.2. H_2/α-Al_2O_3 Interactions. We exposed A_Al_I, A_O_I, M_Al, M_O, C_Al_I, C_Al_II, and C_O_I to H_2 gas-phase molecules at the same concentration (Table 5).

Table 5. Properties of the H_2/α-Al_2O_3 Interactive Systems[a]

Surface Name	Surface O Density (Å^{-2})	H_2 / Unit Area (Å^{-2})	Surface Reactivity
C_Al_II	0.050	0.126 H_2	None
C_Al_I	0.101	0.126 H_2	None
A_Al_I	0.083	0.126 H_2	Small
*A_O_I	0.099	0.126 H_2	
M_Al	0.096	0.126 H_2	
M_O	0.128	0.126 H_2	
C_O_I	0.151	0.126 H_2	Large

These systems were heated (0.013 K/fs) from 300 K, then held at 1275 K for 1 ns, and finally cooled (0.0067 K/fs) to 300 K in the NVT ensemble. The simulation box parameters and the side views of A_Al_I, A_O_I, M_Al, M_O, and C_O_I are shown in Figure 11a. For the simulation of the surface O removals on C_O_I with a reduced H−H σ bond energy parameter in the force field, we heated the system up

https://doi.org/10.1021/acs.jpcc.4c04669
J. Phys. Chem. C 2024, 128, 18767−18781

from 300 to 1275 K using the NPT ensemble, then held it in the NVT ensemble at 1275 K for over 1.5 ns, and finally cooled it down to 300 K in the NPT ensemble. H_2O molecules as the reaction products were removed continually from the system, while H_2 molecules were added continually during the isothermal treatment at 1275 K. The frequencies of both adding H_2 and removing H_2O were 50,000 iterations.

5. RESULTS AND DISCUSSIONS

5.1. H_2O/α-Al_2O_3 (0001) Interactions. *5.1.1. Ordered α-Al_2O_3 (0001) Surfaces.* C_Al_I and C_Al_II planes adsorb gas-phase H_2O molecules in a broad temperature range and release them as the temperature increases. Figure 6 provides

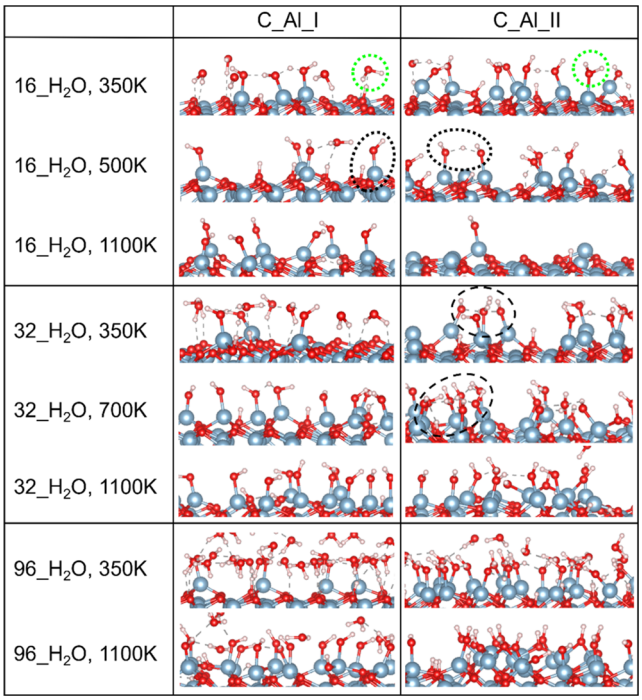

Figure 6. Green dotted circle in 16_H_2O, 350 K, C_Al_I indicates the attraction of a gas-phase H_2O to the surface by hydrogen bonding. The green dotted circle in 16_H_2O, 350 K, C_Al_II indicates the molecular adsorption of an H_2O molecule to the surface. Black dotted circles in 16_H_2O, 500 K (C_Al_I and C_Al_II) indicate two types of chemisorption of H_2O, the complete hydrolysis and the O_xH_y clustering, respectively. Black dashed circles in 32_H_2O, 350 and 700 K (C_Al_II) indicate heavily clustered O_xH_y.

MD snapshots of selected H_2O/α-Al_2O_3 (0001) systems at different temperatures and highlights various types of H_2O/α-Al_2O_3 (0001) interactive events. There are two types of chemisorption reactions that involve the dissociation of H_2O molecules: complete hydrolysis and O_xH_y clustering. The former involves a molecularly adsorbed H_2O molecule transferring a proton to a nearby surface oxygen through either 1−2 or 1−4 pathways, producing two surface hydroxyls. The latter involves a molecularly adsorbed H_2O molecule sharing a proton with a neighboring hydroxyl via hydrogen bonding, producing one surface hydroxyl. Overall, C_Al_II forms more O_xH_y clusters than C_Al_I due to the fewer number of surface O to adopt transferred proton from H_2O molecules, which is consistent with the DFT investigations on H_2O/Al (111) systems done by Guo et al., suggesting that the preadsorbed O plays an important role in dissociating H_2O on clean Al (111).[61]

The in-plane hydrogen bonding between adsorbed H_2O molecules allows proton transferring along a linear route (Figure 6, 16_H_2O, 350 K, C_Al_I) or a near-closed loop (Figure 6, 32_H_2O, 700 K, C_Al_II). The hydrogen bonding between the surface and the H_2O molecules that are not directly adsorbed prevents the H_2O from moving further, which in turn traps more H_2O molecules via interwater hydrogen bonding and eventually results in the formation of an H_2O layer above the surface (Figure 6, 32_H_2O, 350 K, C_Al_I). When the H_2O concentration is high enough, H_2O molecules tend to form multiple layers above the surface (Figure 6, 96_H_2O, 350 K, C_Al_I). These observations could be considered as great extensions to the proton transferring events discussed by Hass et al. using first-principle molecular dynamics on smaller systems.[62]

However, no H_2 generations have been observed, which does not entirely agree with the scenario predicted by Lu et al. using DFT and MD simulations for H_2O/γ-Al_2O_3 (110).[63]

Figure 7a,c presents the H_2O chemisorption rates, defined as the ratio of the number of dissociated H_2O to the initial number of H_2O, to quantify the overall reactivity of α-Al_2O_3 (0001) during H_2O exposures at different gas-phase concentrations and temperatures. Figure 7b,d presents the O_xH_y clustering rates, defined as the ratio of the number of protons not forming surface hydroxyls to the initial number of H_2O, which aids in shedding light on the reaction mechanisms. For all of the H_2O concentrations considered in this work, the H_2O chemisorption rates peak at either 500 or 700 K before declining and reaching near-plateaus except for the systems with 16 H_2O molecules, where the H_2O chemisorption rate reincreases at $T \geq 1100$ K. O_xH_y clustering rates exhibit the same trends as the corresponding H_2O chemisorption rates at $T \leq 1100$ K. At $T > 1100$ K, the O_xH_y clustering rates simply drop to very small values. Overall, C_Al_II is more reactive to H_2O than C_Al_I. But half and more of the chemisorbed H_2O on C_Al_II contributes to O_xH_y clustering instead of going through complete hydrolysis, while C_Al_I exhibits the opposite phenomena (Figure 7b,d), since C_Al_II is 100% Al-terminated and has fewer surface O to adopt transferred protons.

Figure 8a depicts the maximum H_2O chemisorption rates on C_Al_I and C_Al_II (at $T < 1100$ K) for different H_2O concentrations. The maximum H_2O chemisorption rates peak with 32 and 48 H_2O for C_Al_I and C_Al_II, respectively, with higher values for C_Al_II than C_Al_I. Figure 8b shows the corresponding coverages of chemisorbed H_2O, defined as the maximum number of dissociated H_2O divided by the number of surface Al species. The maximum coverages of chemisorbed H_2O increase with the H_2O concentrations and reach near-plateaus when the initial H_2O numbers ≥ 48 for both C_Al_I and C_Al_II, but with higher values for C_Al_I than C_Al_II. Neither C_Al_I nor C_Al_II has been fully hydroxylated, with saturation converges as ~ 0.73 and ~ 0.60, respectively.

In the system at a low H_2O concentration, H_2O molecules undergo 1−2 or 1−4 pathways to hydroxylate the surface (Figure 9e). When the H_2O concentration increases moderately, gas-phase H_2O molecules act like catalysts to facilitate surface hydroxylation, which is called autocatalysis (Figure 9f). Such catalyzed dissociation is also mentioned or suggested by other computational studies.[62,64,65] When the

https://doi.org/10.1021/acs.jpcc.4c04669
J. Phys. Chem. C 2024, 128, 18767−18781

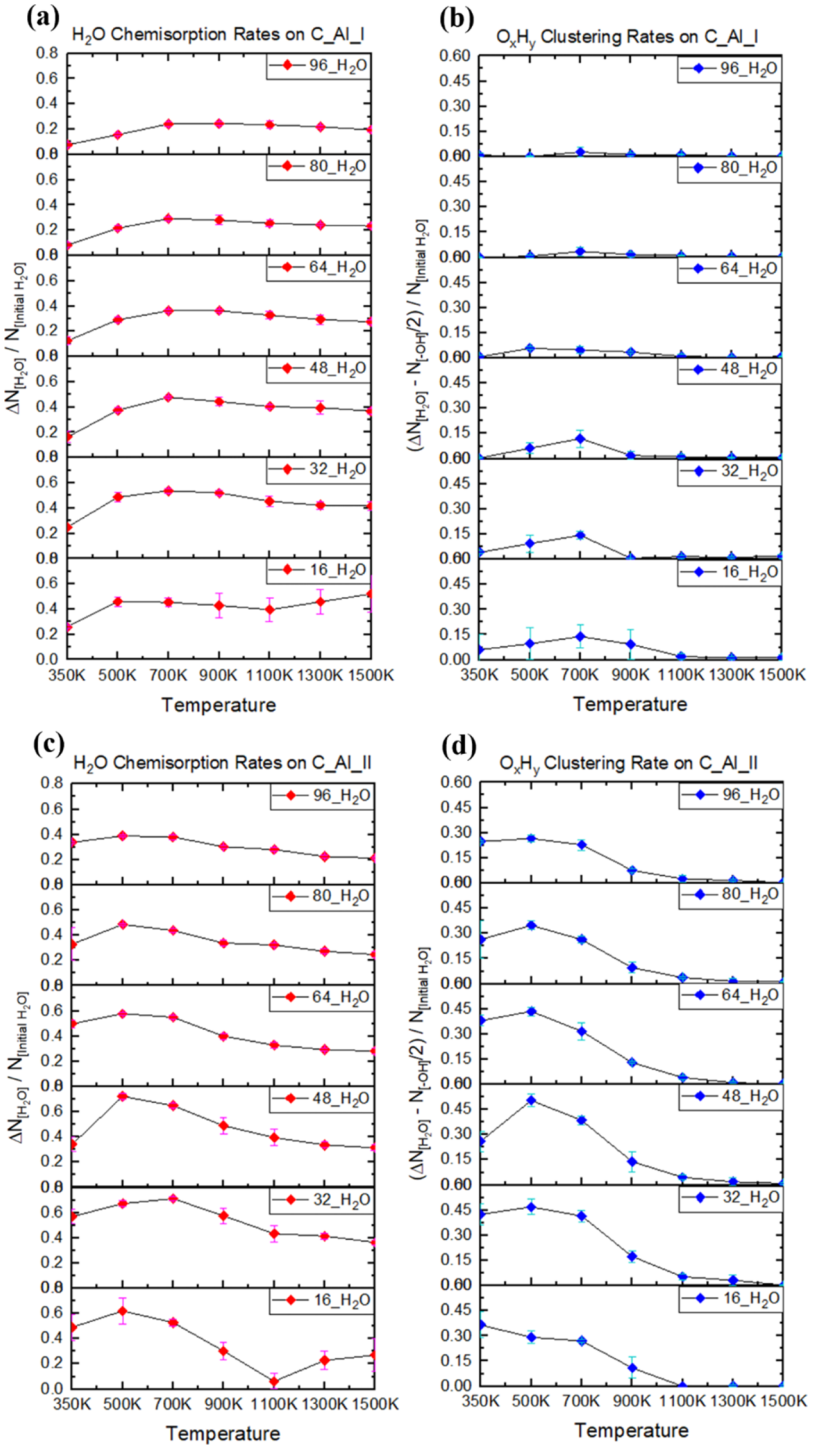

Figure 7. Panels (a) and (c) are H_2O chemisorption rates for C_Al_I and C_Al_II, respectively. The H_2O chemisorption rate is defined as the ratio of the number of dissociated H_2O to the initial number of H_2O. Panels (b) and (d) are O_xH_y clustering rates for C_Al_I and C_Al_II, respectively. The O_xH_y clustering rate is defined as the ratio of the number of protons not forming surface hydroxyls to the initial number of H_2O.

H_2O concentration keeps increasing, extra H_2O molecules aggregate above the surface and form a protecting layer to prevent further hydroxylation, which is called surface poisoning (Figure 9g). Increasing the temperature to the most suitable value mitigates surface poisoning at high H_2O concentrations, but surface hydroxyls still become dense enough to prevent further hydrolysis starting from 48_H_2O systems. Figure 9d intuitively shows that the 96_H_2O system does not have an obvious increase of the surface hydroxyl quantity compared to the 48_H_2O system. Extra H_2O molecules are trapped near the layer consisting of surface hydroxyls and shared protons and are unable to reach the surface. Besides, large O_xH_y clusters distort the surface structure, reducing the likelihood of subsequent hydroxylation occurring in their vicinity (Figure 6). The above mechanisms explain why the maximum coverages of chemisorbed H_2O tend to reach near-plateaus (or saturation coverages) and have values smaller than one in both cases (Figure 8b). These also explain the nonlinear

https://doi.org/10.1021/acs.jpcc.4c04669
J. Phys. Chem. C 2024, 128, 18767−18781

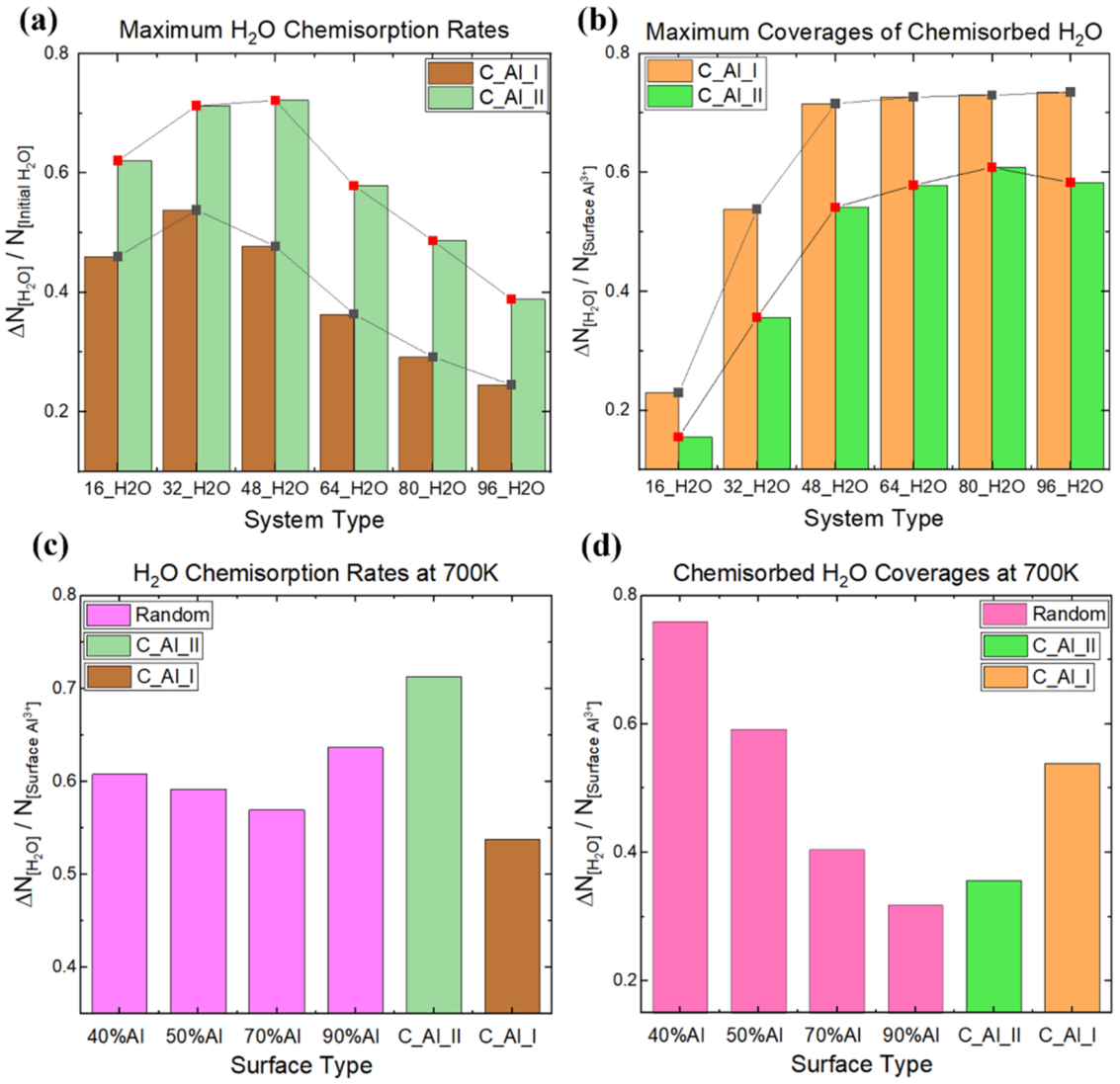

Figure 8. Panels (a) and (b) are the maximum H_2O chemisorption rates and the maximum coverages of chemisorbed H_2O for different H_2O concentrations in H_2O/α-Al_2O_3 (0001) systems, respectively. Panels (c) and (d) compare the random and ordered α-Al_2O_3 (0001) surfaces regarding the H_2O chemisorption rates and the chemisorbed H_2O coverages at 700 K, respectively.

relationships between the maximum H_2O chemisorption rates and the H_2O concentrations in Figure 8a, where a moderate H_2O concentration increase improves the maximum H_2O chemisorption rate, while an excessive increase in the former reduces the latter. Since the surface hydroxyl density plays a nonnegligible role in determining the saturation quantity of surface hydroxyls, C_Al_II (100% Al termination) can barely produce more hydroxyls than C_Al_I (50% Al termination) by the number equal or more than that of the exceeded surface Al. So, C_Al_II has a lower saturation coverage of chemisorbed H_2O than C_Al_I.

Low energy barriers for the hydrolysis on Al-terminated α-Al_2O_3 (0001) (Figure 3) allow H_2O molecules to dissociate at temperatures as low as 350 K. When the temperature increases over 500 or 700 K, a system experiences H_2O desorption, where the proton bonded to the surface O transfers back to the neighboring hydroxyl bonded to the surface Al and reforms a H_2O molecule. Protons contributed to O_xH_y clustering are more easy to reform gas-phase H_2O. Since the H_2O chemisorption on C_Al_II relies more on O_xH_y clustering than complete hydrolysis, Figure 7 shows steeper drops in H_2O chemisorption rates for C_Al_II than C_Al_I upon reaching the temperatures where H_2O desorption starts to occur. However, increasing temperatures cannot eliminate surface hydroxyls. Due to combined mechanisms of proton transfer and H_2O desorption (Figure 9b), the remaining surface hydroxyls become distantly positioned at elevated temperatures, hindering the proton transfer necessary for releasing H_2O between neighboring hydroxyls. Besides, when the temperature is high enough, lattice distortions in Figure 9a or c occur, where the surface O with a transferred proton attached is uptilted, driving the transferred proton farther away from the neighboring hydroxyl and making H_2O reformation less likely to happen. This explains why systems with 16 H_2O molecules exhibit reincreasing trends in H_2O chemisorption rates upon reaching 1100 K or higher. H_2O chemisorption still happens at $T \geq 1100$ K, while H_2O desorption is prohibited due to lattice distortions. When the surface hydroxyl coverage is smaller than the saturation value, the surface is still able to chemisorb H_2O molecules, and the chemisorbed H_2O molecules are kept on the surface at high temperatures.

https://doi.org/10.1021/acs.jpcc.4c04669
J. Phys. Chem. C 2024, 128, 18767−18781

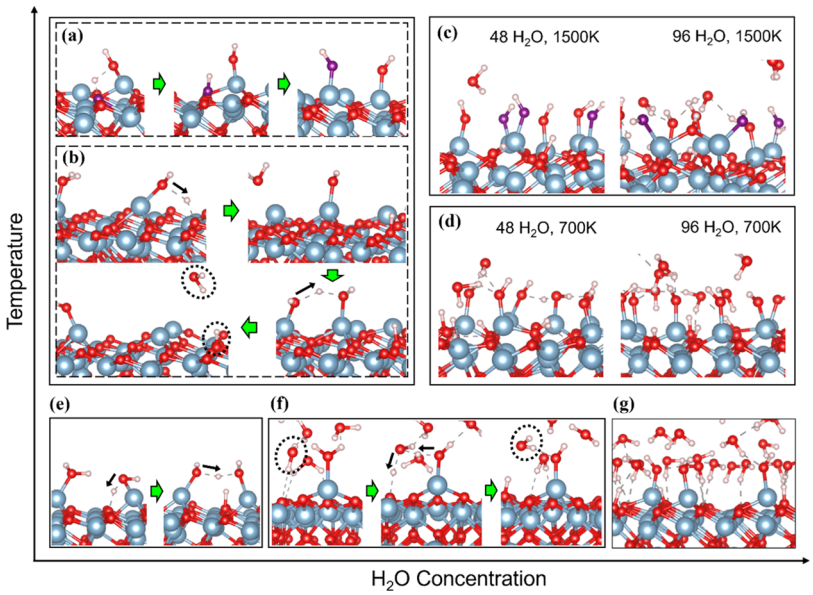

Figure 9. (a) Lattice distortion of the α-Al_2O_3 (0001) surface happens at high temperatures and low H_2O concentrations. The purple-colored O is from the surface but is driven upward due to the lattice distortion. (b) Proton transfers combined with the H_2O reformation at high temperatures and low H_2O concentrations. (c) Comparison of surface hydroxyls between systems with 48 and 96 initial H_2O molecules at 1500 and (d) 700 K. (e) H_2O chemisorption mechanisms at low temperatures and low H_2O concentrations. (f) Autocatalysis of H_2O dissociation at moderate H_2O concentrations. (g) Surface poisoning at high H_2O concentrations.

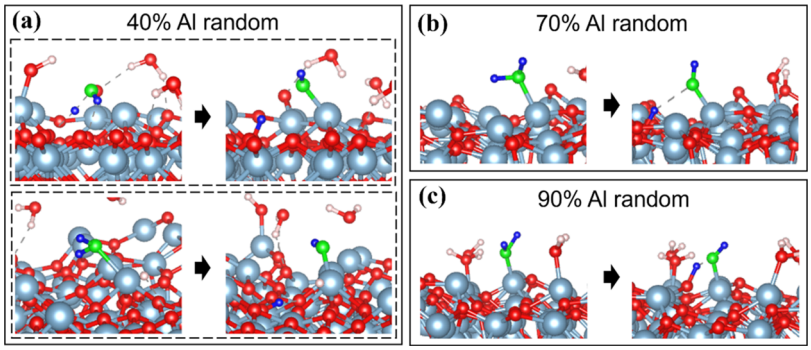

Figure 10. Panel (a) indicates two H_2O dissociation events at the 40% Al-terminated random surface. Panel (b) indicates O−H bond dissociation of a physiosorbed H_2O on the 70% Al-terminated random surface. Panel (c) indicates H_2O dissociation through 1−4 pathway at the 90% Al-terminated random surface. Dissociated H_2O molecules are colored green (for O) and blue (for H).

5.1.2. Random α-Al_2O_3 (0001) Surfaces. The H_2O chemisorption rates and the chemisorbed H_2O coverages of random surfaces at 700 K are shown in Figure 8c,d, respectively. Random surfaces exhibit decreasing trends in the H_2O chemisorption rates and the chemisorbed H_2O coverages from 40% to 70% Al-terminations. The randomly distributed surface Al species induce surface distortions, leading to the H_2O dissociation deviating from 1−2 and 1−4 pathways (Figure 10a,b). Figure 10a indicates two H_2O dissociation events occurring at the 40% Al-terminated random surface, where the O-Al bond formation can happen either before or simultaneously with proton transferring to the surface O. On the other hand, the 70% Al-terminated random surface is smoother (Figure S3), where the H_2O dissociation always happens after the oxygen in H_2O bonds to the surface Al (Figure 10b). The 90% Al-terminated random surface has a higher H_2O chemisorption rate than the 70% Al-terminated one because the former recovers the regular (1−2 or 1−4) H_2O dissociation pathways (Figure 10c). However, the 90% Al-terminated random surface exhibits a lower chemisorbed H_2O coverage than all of the other surfaces because the H_2O concentration is not high enough to trigger a high chemisorbed H_2O coverage considering the dense Al coverage of the surface, which is the same reason for C_Al_II having a relatively low chemisorbed H_2O coverage. The comparison between the 50% Al-terminated random surface and C_Al_I may suggest that the random surface is more reactive than the ordered surface with the same Al coverage.

5.2. H_2/α-Al_2O_3 Interactions. Figure 11b shows the time evolutions of the surface hydroxyl formation rates, defined as the ratio of the number of surface hydroxyls to the initial number of H_2 for seven different α-Al_2O_3 surfaces. C_Al_II, C_Al_I, A_Al_I, A_O_I, M_Al, M_O, and C_O_I exhibit an increasing trend in their reactivity to the gas-phase H_2, based on the slopes of the corresponding curves at the early stage (<0.2 ns) in Figure 11b. There are no curves for C_Al_II and C_Al_I in Figure 11b because both surfaces remain non-reactive to H_2 throughout the simulations. The reactivity to H_2 is affected by the crystallographic plane and the surface O coverage (Table 5). The surface becomes more reactive to H_2

https://doi.org/10.1021/acs.jpcc.4c04669
J. Phys. Chem. C 2024, 128, 18767−18781

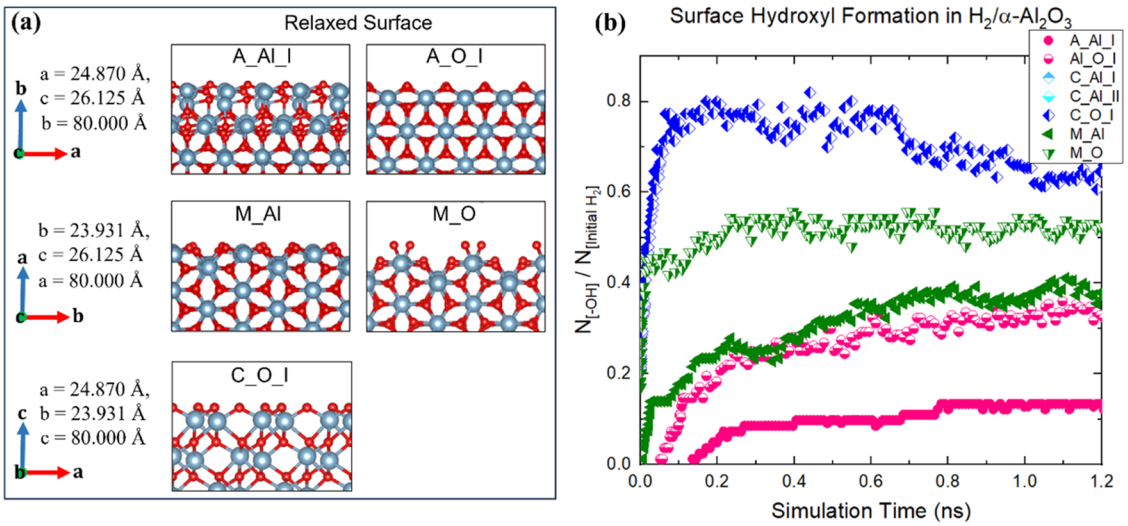

Figure 11. (a) Models of α-Al_2O_3 substrates used to study H_2/α-Al_2O_3. Surface names correspond to those in Table 2 and Figure 2. M_O is 50% O-terminated α-Al_2O_3 $(10\bar{1}0)$. (b) Time evolution of hydroxyl formation rates for α-Al_2O_3 substrates under H_2 preannealing.

when it has a higher surface O coverage, since the two H atoms in an H_2 molecule can bond with two surface O atoms simultaneously with a weak interaction still maintained between the two H atoms, thus preventing complete H_2 dissociation and reducing the energy barrier for surface hydroxylation. C_O_I is fully O-terminated and has the highest surface O coverage, exhibiting the highest reactivity to H_2. On the other hand, C_Al_I remains nonreactive to H_2, even though it has a similar surface O coverage to A_O_I or M_Al. Meanwhile, M_Al is more reactive to H_2 than A_O_I. These can be explained by the thermodynamic stability trend of the crystallographic planes, C > A > M, where the reduced surface stability increases the surface energy, consequently enhancing the surface reactivity to H_2.

C_O_I has an obvious drop in its hydroxyl formation rate at the later stage (>0.7 ns) because a significant number of H_2O molecules are formed at the consumption of surface hydroxyls (Figure S5). M_O initiates H_2O formation with the highest rate at the beginning (<0.2 ns) and lowers the H_2O formation rate after the early stage (>0.2 ns) (Figure S5). Then, the hydroxyl formation rate of M_O exhibits a near-plateau. This suggests a balanced mode between H_2O formation and H_2 dissociation on M_O after ∼ 0.2 ns. In the overall increasing trend of the M_Al hydroxyl formation rate, there exist fluctuations; the hydroxyl formation rate exhibits downward curves in 0.23−0.47 and 0.82−1.1 ns (Figure 11b). These downward curves correspond to the upward curves in the H_2O formation rate of M_Al in Figure S5. These fluctuations are caused by the combined effect of H_2O formation and hydrolysis at surfaces that are partially hydroxylated and partially Al-terminated. In this scenario, the H_2O molecules formed from surface hydroxyls can bind to and rehydroxylate the surface.

To explore the reaction kinetics of C_Al_I in the H_2 gas-phase exposure, we artificially reduced the energy barrier of H_2 dissociation. The force field parameter for the H−H σ bond energy was gradually lowered from the original value of 165 to 140 kcal/mol by 5 kcal/mol while the rest of the parameters in the force field were kept the same as before. Correspondingly, the energy barriers of H_2 dissociations using ff_165, ff_160, ff_155, ff_150, ff_145, and ff_140 are 45, 43, 36.4, 32.4, 29.3, and 25.6 kcal/mol, respectively (Figure 12a). We used the calculated energy barriers to predict the initiation time of H_2 dissociation on C_Al_I for different values of the H−H σ bond energy parameter. The change of the H_2 dissociation reaction rate constant (demoted as k), defined as the inverse of the waiting time to observe the first H_2 dissociation event, with respect to the H_2 dissociation energy barrier at 1275 K, is presented in Figure 12b in the natural logarithm form ($\ln k$). Only the datapoints for ff_140, ff_145, ff_150, and ff_155 are shown because no H_2 dissociation events occurred using ff_160 and ff_165 within the simulation time, which was 2 ns. Based on the linear relationship between $\ln k$ and the energy barrier, the predicted waiting time of observing H_2 dissociation is ∼ 5 ns for the original parameter of 165 kcal/mol under the current system conditions.

We used ff_140 to accelerate the surface O removal process during the H_2 preannealing of C_O_I. To mimic experimental conditions, we applied constant H_2 flows and removed H_2O simultaneously in the H_2/C_O_I system. Figure 12c,d shows the numerical analysis of chemical species in H_2/C_O_I and the visualizations of C_O_I surface at different stages of the simulation, respectively. After ∼ 1.5 ns, the surface O removal process tends to cease (Figure 12c), and the surface structure is comparable to that of C_Al_II after H_2 preannealing (Figure S4f). At 1.5 ns, there are still ∼ 6.67% of hydroxyls left. When surface hydroxyls become sparsely distributed as the simulation goes on, an H_2 molecule transfers one proton to a subsurface O and transfers the other to an existing hydroxyl to form H_2O, which in turn creates a new hydroxyl. Once the proton is bonded to subsurface O, it can hardly be removed by H_2 again. But it can transfer to a neighboring hydroxyl bonded to a surface Al and form H_2O, which is not a highly possible event when the existing hydroxyls are getting sparse (Figure S6).

6. CONCLUSIONS

This study introduces a newly parametrized ReaxFF reactive force field designed to investigate how the surface termination and the crystallographic plane influence the dissociation behaviors of H_2O and H_2 on α-Al_2O_3 substrates. The force field reproduces the surface energy trend for stoichiometric α-Al_2O_3 as C < R < A < M and achieves a lower H_2O

https://doi.org/10.1021/acs.jpcc.4c04669
J. Phys. Chem. C 2024, 128, 18767−18781

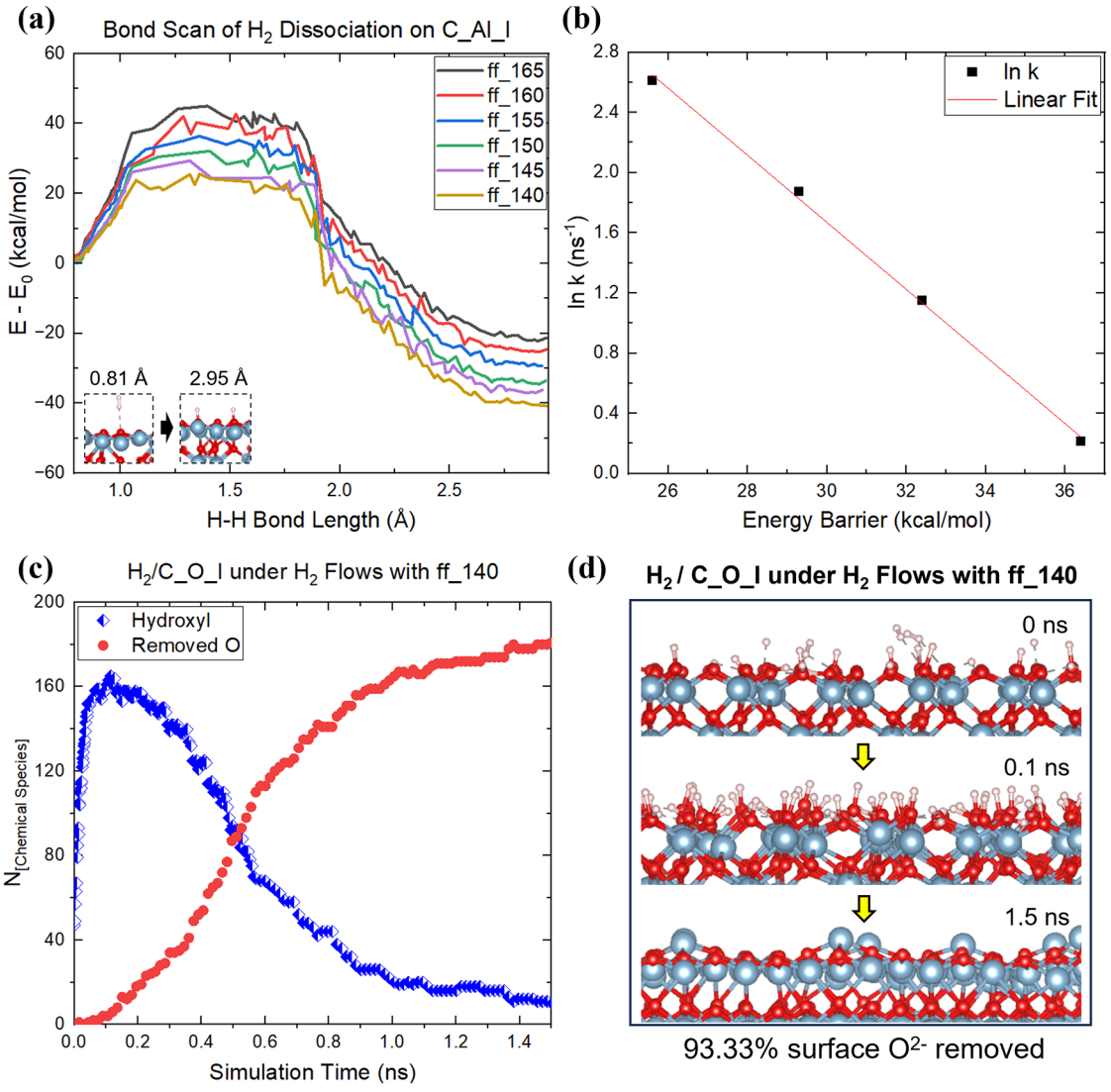

Figure 12. (a) Energy profiles of H_2 dissociations on C_Al_I with the H−H σ bond energy parameter set as 165 kcal/mol, 160 kcal/mol, 155 kcal/mol, 150 kcal/mol, 145 kcal/mol, and 140 kcal/mol, labeled as ff_165, ff_160, ff_155, ff_150, ff_145, and ff_140, respectively. 165 kcal/mol is the original value. (b) Relationship between the natural logarithm of the H_2 dissociation reaction rate constant and the energy barrier of H_2 dissociation. (c) Numerical evolutions of the surface hydroxyls and the removed surface O under constant H_2 gas flows using ff_140. (d) Surface structures of C_O_I under constant H_2 gas flows with ff_140 at different stages.

dissociation barrier for the 1−4 than the 1−2 pathway, which is consistent with quantum chemical (QC) predictions.[35,36,40,41] Based on the ReaxFF simulations, we indeed observe that the C-plane is the most stable, while the M-plane is the least stable under H_2 preannealing. With similar surface O coverages, the surface reactivity to H_2 exhibits the tread as C < A < M. Also, the H_2 preannealed C-plane surfaces maintain the highest crystallinity compared with A- and M-planes.

The simulations of H_2O/α-Al_2O_3 (0001) reveal that the Al-terminated α-Al_2O_3 (0001) hydroxylated by the H_2O gas phase begins to desorb H_2O molecules once heated up to 500 K or higher. But protons bonded to the surface oxygens transfer between hydroxyls more randomly at elevated temperatures, making the remaining hydroxyls distantly positioned and hindering subsequent H_2O reformations. Consequently, simply increasing the temperature does not fully eliminate surface hydroxyls. Fully hydroxylating the surface is unachievable by simple H_2O gas-phase exposure because either the extra H_2O molecules or the surface hydroxyls, together with the shared protons, will form a protecting layer to prevent further hydroxylation eventually. Our newly developed force field describes the H_2O/α-Al_2O_3 (0001) interaction behavior consistent with published QC studies and corroborates the noninterconvertibility between the Al-terminated and the Gibbsite-like surfaces at the atomic level.[35,36,40−42] Furthermore, our simulations reveal more patterns of H_2O dissociations, including the mechanism of O_xH_y clustering through hydrogen bonding and how it influences the surface hydroxylation and the gas molecule desorption behaviors. We also determined the maximum H_2O chemisorption rates and the maximum degrees of surface hydroxylation based on statistical analyses across different temperatures and H_2O concentrations and demonstrated the importance of water autocatalytic reactions for alumina/water reactivity.

We also developed and tested the accelerated molecular dynamics (MD) simulation of H_2 reaction with 100% O-terminated α-Al_2O_3 (0001). We showed that our accelerated MD simulation, which systematically weakens the H−H bond,

https://doi.org/10.1021/acs.jpcc.4c04669
J. Phys. Chem. C 2024, 128, 18767−18781

renders a surface termination comparable to that of a 100% Al-terminated surface in 1.5 ns, indicating that the accelerated MD simulation can serve as a promising method to reveal the compositional and morphological changes of α-Al_2O_3 surfaces under H_2 preannealing. Our work demonstrates the applicability of the new ReaxFF Al/O/H reactive force field for modeling the surface engineering process of α-Al_2O_3 substrates with various terminations along different crystallographic planes in H_2O/H_2 gas-phase environments. In future work, this force field can be expanded to encompass more intricate interactions between the gas-phase precursors and α-Al_2O_3 substrates during the epitaxy of transition-metal dichalcogenides (TMDs), which govern the growth mechanisms of TMDs on α-Al_2O_3 substrates.

■ ASSOCIATED CONTENT

Supporting Information

The Supporting Information is available free of charge at https://pubs.acs.org/doi/10.1021/acs.jpcc.4c04669.

Illustrations of crystallographic planes A, M, C, and R of α-Al_2O_3 and different surface terminations of A, M, C, and R-planes, of which the surface energies were used as force field training data. Hydroxylation energies and energy barriers of H_2O dissociations through 1−2 and 1−4 pathways on 50% Al-terminated α-Al_2O_3 (0001) calculated by DFT and ReaxFF. Plots of dehydration energies of fully hydroxylated step-terrace α-Al_2O_3 (0001) in both H_2O-rich and O-rich environments calculated by DFT and ReaxFF. Surface structures of random Al-terminated α-Al_2O_3 (0001) after H_2O exposure. Surface structures of Al- or O-terminated α-Al_2O_3 substrates along A, M, and C planes after H_2 preannealing. H_2O formation rates for Al- or O-terminated α-Al_2O_3 substrates along A, M, and C planes during H_2 preannealing. The figure showing sparsely distributed hydroxyls left on an initially O-rich C-plane after H_2 exposure in our accelerated simulation. Force field parameters of the newly developed Al/O/H force field (PDF)

■ AUTHOR INFORMATION

Corresponding Author

Adri C. T. van Duin − *Department of Materials Science and Engineering, The Pennsylvania State University, University Park, Pennsylvania 16802, United States; Department of Mechanical Engineering and 2D Crystal Consortium Material Innovation Platform (2DCC-MIP) Materials Research Institute, The Pennsylvania State University, University Park, Pennsylvania 16802, United States;* orcid.org/0000-0002-3478-4945; Email: acv13@psu.edu

Authors

Yuwei Zhang − *Department of Materials Science and Engineering, The Pennsylvania State University, University Park, Pennsylvania 16802, United States;* orcid.org/0000-0003-0188-1981

Nadire Nayir − *Department of Physics Engineering, Istanbul Technical University, Maslak, Istanbul 34469, Turkey; Department of Mechanical Engineering, The Pennsylvania State University, University Park, Pennsylvania 16802, United States;* orcid.org/0000-0002-3621-2481

Yun Kyung Shin − *Department of Mechanical Engineering, The Pennsylvania State University, University Park, Pennsylvania 16802, United States;* orcid.org/0000-0001-8198-001X

Qian Mao − *Department of Mechanical Engineering and 2D Crystal Consortium Material Innovation Platform (2DCC-MIP) Materials Research Institute, The Pennsylvania State University, University Park, Pennsylvania 16802, United States;* orcid.org/0000-0001-8760-0006

Ga-Un Jeong − *Department of Mechanical Engineering, The Pennsylvania State University, University Park, Pennsylvania 16802, United States*

Chen Chen − *2D Crystal Consortium Material Innovation Platform (2DCC-MIP) Materials Research Institute, The Pennsylvania State University, University Park, Pennsylvania 16802, United States*

Joan M. Redwing − *Department of Materials Science and Engineering, The Pennsylvania State University, University Park, Pennsylvania 16802, United States; 2D Crystal Consortium Material Innovation Platform (2DCC-MIP) Materials Research Institute, The Pennsylvania State University, University Park, Pennsylvania 16802, United States;* orcid.org/0000-0002-7906-452X

Complete contact information is available at: https://pubs.acs.org/10.1021/acs.jpcc.4c04669

Notes

The authors declare no competing financial interest.

■ ACKNOWLEDGMENTS

Financial support was provided by AFOSR MURI Contract No. FA9550-19-1-0008 and the Two-Dimensional Crystal Consortium—Materials Innovation Platform (2DCC-MIP) at Pennsylvania State University under National Science Foundation Cooperative Agreement DMR-2039351.

■ ADDITIONAL NOTE

[a]*A_O_I has a number density of surface O species as 0.083 $Å^{-2}$. The subsurface O is partially exposed and engaged in dissociating H_2 throughout the simulation. Statistics show that around 16.01% of the hydroxyls on Al_O_I are formed using the subsurface O. So, the exposed surface O number density of A_O_I is adopted as 0.099 $Å^{-2}$.

■ REFERENCES

(1) Cranston, R. R.; Lessard, B. H. Metal phthalocyanines: Thin-film formation, microstructure, and physical properties. *RSC Adv.* **2021**, *11* (35), 21716−21737.

(2) Sreehari, S.; George, N. S.; Jose, L. M.; Nandakumar, S.; Subramaniam, R. T.; Aravind, A. A review on 2D transition metal nitrides: Structural and morphological impacts on energy storage and photocatalytic applications. *J. Alloys Compd.* **2023**, *950*, No. 169888.

(3) Di, H.; Jiang, W.; Sun, H.; Zhao, C.; Liao, F.; Zhao, Y. Effects of ITO substrate hydrophobicity on crystallization and properties of MAPbBr3 single-crystal thin films. *ACS Omega* **2020**, *5* (36), 23111−23117.

(4) Amrillah, T.; Duong, M. N.; Chen, Y.-X.; Bitla, Y.; Baqiya, M. A.; Indah Sari, F. N.; Thi Quynh, L.; Hermawan, A.; Simanjuntak, F. M.; Chen, C.-H.; et al. Effects of surface polarity on the structure and magnetic properties of epitaxial h-YMnO3 thin films grown on MgO substrates. *ACS Appl. Electron. Mater.* **2022**, *4* (4), 1603−1610.

(5) Sazideh, M. R.; Ehsani, M. H.; Shahidi, M. M.; Rezagholipour Dizaji, H. Growth mechanism of nano-plates structured SnS films on

different substrates in glancing angle deposition method. *Sci. Rep.* **2022**, *12* (1), No. 17913.
(6) Bianco, E.; Rao, R.; Snure, M.; Back, T.; Glavin, N. R.; McConney, M. E.; Ajayan, P.; Ringe, E. Large-area ultrathin Te films with substrate-tunable orientation. *Nanoscale* **2020**, *12* (23), 12613−12622.
(7) Peng, L. E.; Yao, Z.; Yang, Z.; Guo, H.; Tang, C. Y. Dissecting the role of substrate on the morphology and separation properties of thin film composite polyamide membranes: seeing is believing. *Environ. Sci. Technol.* **2020**, *54* (11), 6978−6986.
(8) Zhu, H.; Nayir, N.; Choudhury, T. H.; Bansal, A.; Huet, B.; Zhang, K.; Puretzky, A. A.; Bachu, S.; York, K.; Mc Knight, T. V.; et al. Step engineering for nucleation and domain orientation control in WSe2 epitaxy on c-plane sapphire. *Nat. Nanotechnol.* **2023**, *18* (11), 1295−1302.
(9) Pradhan, D.; Gartia, A.; Ghosh, S. P.; Sahoo, K. K.; Bose, G.; Kar, J. P. Impact of H2 gas on the properties of MoS2 thin films deposited by sulfurization of Mo thin films. *Micro Nano Lett.* **2021**, *16* (11), 525−532.
(10) Najmaei, S.; Yuan, J.; Zhang, J.; Ajayan, P.; Lou, J. Synthesis and defect investigation of two-dimensional molybdenum disulfide atomic layers. *Acc. Chem. Res.* **2015**, *48* (1), 31−40.
(11) Levin, I.; Brandon, D. Metastable alumina polymorphs: crystal structures and transition sequences. *J. Am. Ceram. Soc.* **1998**, *81* (8), 1995−2012.
(12) Meyer, J.; Görrn, P.; Bertram, F.; Hamwi, S.; Winkler, T.; Johannes, H.-H.; Weimann, T.; Hinze, P.; Riedl, T.; Kowalsky, W. Al2O3/ZrO2 nanolaminates as ultrahigh gas-diffusion barriers-a strategy for reliable encapsulation of organic electronics. *Adv. Mater.* **2009**, *21* (18), 1845−1849.
(13) Li, N.; Wei, Z.; Zhao, J.; Wang, Q.; Shen, C.; Wang, S.; Tang, J.; Yang, R.; Shi, D.; Zhang, G. Atomic layer deposition of Al2O3 directly on 2D materials for high-performance electronics. *Adv. Mater. Interfaces* **2019**, *6* (10), No. 1802055.
(14) Amano, H.; Sawaki, N.; Akasaki, I.; Toyoda, Y. Metalorganic vapor phase epitaxial growth of a high quality GaN film using an AlN buffer layer. *Appl. Phys. Lett.* **1986**, *48* (5), 353−355.
(15) An, Y.; Dai, L.; Wu, Y.; Wu, B.; Zhao, Y.; Liu, T.; Hao, H.; Li, Z.; Niu, G.; Zhang, J.; et al. Epitaxial growth of β-Ga2O3 thin films on Ga2O3 and Al2O3 substrates by using pulsed laser deposition. *J. Adv. Dielectr.* **2019**, *09* (04), No. 1950032.
(16) Dong, J.; Zhang, L.; Dai, X.; Ding, F. The epitaxy of 2D materials growth. *Nat. Commun.* **2020**, *11* (1), No. 5862.
(17) Pishchik, V.; Lytvynov, L. A.; Dobrovinskaya, E. R.Application of Sapphire. *Sapphire: Material, Manufacturing, Applications* 2009, pp 1−54.
(18) Dumcenco, D.; Ovchinnikov, D.; Marinov, K.; Lazic, P.; Gibertini, M.; Marzari, N.; Sanchez, O. L.; Kung, Y.-C.; Krasnozhon, D.; Chen, M.-W.; et al. Large-area epitaxial monolayer MoS2. *ACS Nano* **2015**, *9* (4), 4611−4620.
(19) Aljarb, A.; Cao, Z.; Tang, H.-L.; Huang, J.-K.; Li, M.; Hu, W.; Cavallo, L.; Li, L.-J. Substrate lattice-guided seed formation controls the orientation of 2D transition-metal dichalcogenides. *ACS Nano* **2017**, *11* (9), 9215−9222.
(20) Wang, Q.; Li, N.; Tang, J.; Zhu, J.; Zhang, Q.; Jia, Q.; Lu, Y.; Wei, Z.; Yu, H.; Zhao, Y.; et al. Wafer-scale highly oriented monolayer MoS2 with large domain sizes. *Nano Lett.* **2020**, *20* (10), 7193−7199.
(21) Li, T.; Guo, W.; Ma, L.; Li, W.; Yu, Z.; Han, Z.; Gao, S.; Liu, L.; Fan, D.; Wang, Z.; et al. Epitaxial growth of wafer-scale molybdenum disulfide semiconductor single crystals on sapphire. *Nat. Nanotechnol.* **2021**, *16* (11), 1201−1207.
(22) Liu, L.; Li, T.; Ma, L.; Li, W.; Gao, S.; Sun, W.; Dong, R.; Zou, X.; Fan, D.; Shao, L.; et al. Uniform nucleation and epitaxy of bilayer molybdenum disulfide on sapphire. *Nature* **2022**, *605* (7908), 69−75.
(23) Momeni, K.; Sakib, N.; Figueroa, D. E. C.; Paul, S.; Chen, C. Y.; Lin, Y.-C.; Robinson, J. A. Combined Experimental and Computational Insight into the Role of Substrate in the Synthesis of Two-Dimensional WSe2. *ACS Appl. Mater. Interfaces* **2024**, 6644−6652, DOI: 10.1021/acsami.3c16761.
(24) Paul, S.; Torsi, R.; Robinson, J. A.; Momeni, K. Effect of the Substrate on MoS2 Monolayer Morphology: An Integrated Computational and Experimental Study. *ACS Appl. Mater. Interfaces* **2022**, *14*, 18835−18844, DOI: 10.1021/acsami.2c03471.
(25) Chen, C.; Trainor, N.; Kumari, S.; Myja, H.; Kümmell, T.; Zhang, Z.; Zhang, Y.; Bisht, A.; Sadaf, M. U. K.; Sakib, N. U.; et al. Effect of growth temperature on the microstructure and properties of epitaxial MoS2 monolayers grown by metalorganic chemical vapor deposition. *J. Vac. Sci. Technol., A* **2024**, *42* (2), No. 022201, DOI: 10.1116/6.0003296.
(26) Park, Y.; Ahn, C.; Ahn, J.-G.; Kim, J. H.; Jung, J.; Oh, J.; Ryu, S.; Kim, S.; Kim, S. C.; Kim, T.; Lim, H. Critical role of surface termination of sapphire substrates in crystallographic epitaxial growth of MoS2 using inorganic molecular precursors. *ACS Nano* **2023**, *17* (2), 1196−1205.
(27) Li, H.; Li, Y.; Aljarb, A.; Shi, Y.; Li, L.-J. Epitaxial growth of two-dimensional layered transition-metal dichalcogenides: growth mechanism, controllability, and scalability. *Chem. Rev.* **2018**, *118* (13), 6134−6150.
(28) Millard, T. S.; Genco, A.; Alexeev, E. M.; Randerson, S.; Ahn, S.; Jang, A.; Shin, H. S.; Tartakovskii, A. Large area chemical vapour deposition grown transition metal dichalcogenide monolayers automatically characterized through photoluminescence imaging. 2020.
(29) Momeni, K.; Ji, Y.; Nayir, N.; Sakib, N.; Zhu, H.; Paul, S.; Choudhury, T. H.; Neshani, S.; van Duin, A. C. T.; Van Duin, A. C.; Redwing, J. M. A computational framework for guiding the MOCVD-growth of wafer-scale 2D materials. *npj Comput. Mater.* **2022**, *8* (1), 240.
(30) Guo, Y.; Hu, Y.; Yuan, Q. Synthesis of two-dimensional materials: How computational studies can help? *Wiley Interdiscip. Rev.: Comput. Mol. Sci.* **2023**, *13* (2), No. e1635.
(31) Kandybka, I.; Groven, B.; Medina Silva, H.; Sergeant, S.; Nalin Mehta, A.; Koylan, S.; Shi, Y.; Banerjee, S.; Morin, P.; Delabie, A. Chemical Vapor Deposition of a Single-Crystalline MoS2 Monolayer through Anisotropic 2D Crystal Growth on Stepped Sapphire Surface. *ACS Nano* **2024**, *18*, 3173−3186, DOI: 10.1021/acsnano.3c09364.
(32) Chen, L.; Liu, B.; Ge, M.; Ma, Y.; Abbas, A. N.; Zhou, C. Step-edge-guided nucleation and growth of aligned WSe2 on sapphire via a layer-over-layer growth mode. *ACS Nano* **2015**, *9* (8), 8368−8375.
(33) Causà, M.; Dovesi, R.; Pisani, C.; Roetti, C. Ab initio characterization of the (0001) and (1010) crystal faces of α-alumina. *Surf. Sci.* **1989**, *215* (1−2), 259−271.
(34) Guo, J.; Ellis, D.; Lam, D. Electronic structure and energetics of sapphire (0001) and (1$\bar{1}$ 02) surfaces. *Phys. Rev. B: Condens. Matter Mater. Phys.* **1992**, *45* (23), 13647.
(35) Sun, J.; Stirner, T.; Matthews, A. Structure and surface energy of low-index surfaces of stoichiometric α-Al2O3 and α-Cr2O3. *Surf. Coat. Technol.* **2006**, *201* (7), 4205−4208.
(36) Kurita, T.; Uchida, K.; Oshiyama, A. Atomic and electronic structures of α-Al 2 O 3 surfaces. *Phys. Rev. B: Condens. Matter Mater. Phys.* **2010**, *82* (15), No. 155319.
(37) Hütner, J. I.; Conti, A.; Kugler, D.; Mittendorfer, F.; Kresse, G.; Schmid, M.; Diebold, U.; Balajka, J. Stoichiometric reconstruction of the Al2O3 (0001) surface. *Science* **2024**, *385* (6714), 1241−1244.
(38) Knözinger, H.; Ratnasamy, P. Catalytic aluminas: surface models and characterization of surface sites. *Catal. Rev.: Sci. Eng.* **1978**, *17* (1), 31−70.
(39) Thiel, P. A.; Madey, T. E. The interaction of water with solid surfaces: Fundamental aspects. *Surf. Sci. Rep.* **1987**, *7* (6−8), 211−385.
(40) Ranea, V. A.; Carmichael, I.; Schneider, W. F. DFT Investigation of Intermediate Steps in the Hydrolysis of α-Al2O3 (0001). *J. Phys. Chem. C* **2009**, *113* (6), 2149−2158.
(41) Wang, B.; Hou, H.; Luo, Y.; Li, Y.; Zhao, Y.; Li, X. Density functional/all-electron basis set slab model calculations of the adsorption/dissociation mechanisms of water on α-Al2O3 (0001) surface. *J. Phys. Chem. C* **2011**, *115* (27), 13399−13411.

(42) Yue, Y.; Melani, G.; Kirsch, H.; Paarmann, A.; Saalfrank, P.; Campen, R. K.; Tong, Y. Structure and reactivity of α-Al2O3 (0001) surfaces: how do Al−I and gibbsite-like terminations interconvert? *J. Phys. Chem. C* **2022**, *126* (31), 13467−13476.
(43) Boily, J.-F.; Fu, L.; Tuladhar, A.; Lu, Z.; Legg, B. A.; Wang, Z. M.; Wang, H. Hydrogen bonding and molecular orientations across thin water films on sapphire. *J. Colloid Interface Sci.* **2019**, *555*, 810−817.
(44) Zhang, X.; Arges, C. G.; Kumar, R. Computational Investigations of the Water Structure at the α-Al2O3 (0001)−Water Interface. *J. Phys. Chem. C* **2023**, *127* (31), 15600−15610.
(45) Nayir, N.; Shin, Y. K.; Wang, Y.; Sengul, M. Y.; Hickey, D. R.; Chubarov, M.; Choudhury, T. H.; Alem, N.; Redwing, J.; Crespi, V. H.; van Duin, A. C. T. A ReaxFF Force Field for 2D-WS2 and Its Interaction with Sapphire. *J. Phys. Chem. C* **2021**, *125* (32), 17950−17961.
(46) Nayir, N.; Wang, Y.; Ji, Y.; Choudhury, T. H.; Redwing, J. M.; Chen, L.-Q.; Crespi, V. H.; van Duin, A. C. Theoretical modeling of edge-controlled growth kinetics and structural engineering of 2D-MoSe2. *Mater. Sci. Eng.: B* **2021**, *271*, No. 115263.
(47) Nayir, N.; Wang, Y.; Shabnam, S.; Hickey, D. R.; Miao, L.; Zhang, X.; Bachu, S.; Alem, N.; Redwing, J.; Crespi, V. H.; van Duin, A. C. T. Modeling for structural engineering and synthesis of two-dimensional WSe2 using a newly developed Reaxff reactive force field. *J. Phys. Chem. C* **2020**, *124* (51), 28285−28297.
(48) Ostadhossein, A.; Rahnamoun, A.; Wang, Y.; Zhao, P.; Zhang, S.; Crespi, V. H.; Van Duin, A. C. ReaxFF reactive force-field study of molybdenum disulfide (MoS2). *J. Phys. Chem. Lett.* **2017**, *8* (3), 631−640.
(49) van Duin, A. C. T.; Dasgupta, S.; Lorant, F.; Goddard, W. A. ReaxFF: a reactive force field for hydrocarbons. *J. Phys. Chem. A* **2001**, *105* (41), 9396−9409.
(50) Mao, Q.; Feng, M.; Jiang, X. Z.; Ren, Y.; Luo, K. H.; van Duin, A. C. Classical and reactive molecular dynamics: Principles and applications in combustion and energy systems. *Prog. Energy Combust. Sci.* **2023**, *97*, No. 101084.
(51) Mao, Q.; Zhang, Y.; Kowalik, M.; Nayir, N.; Chandross, M.; van Duin, A. C. Oxidation and hydrogenation of monolayer MoS2 with compositing agent under environmental exposure: The ReaxFF Mo/Ti/Au/O/S/H force field development and applications. *Front. Nanotechnol.* **2022**, *4*, No. 1034795.
(52) Nayir, N.; Mao, Q.; Wang, T.; Kowalik, M.; Zhang, Y.; Wang, M.; Dwivedi, S.; Jeong, G.-U.; Shin, Y. K.; van Duin, A. C. Modeling and simulations for 2D materials: a ReaxFF perspective. *2D Mater.* **2023**, *10*, No. 032002, DOI: 10.1088/2053-1583/acd7fd.
(53) Wen, J.; Ma, T.; Zhang, W.; Psofogiannakis, G.; van Duin, A. C.; Chen, L.; Qian, L.; Hu, Y.; Lu, X. Atomic insight into tribochemical wear mechanism of silicon at the Si/SiO2 interface in aqueous environment: Molecular dynamics simulations using ReaxFF reactive force field. *Appl. Surf. Sci.* **2016**, *390*, 216−223.
(54) Liang, T.; Shin, Y. K.; Cheng, Y.-T.; Yilmaz, D. E.; Vishnu, K. G.; Verners, O.; Zou, C.; Phillpot, S. R.; Sinnott, S. B.; Van Duin, A. C. Reactive potentials for advanced atomistic simulations. *Annu. Rev. Mater. Res.* **2013**, *43*, 109−129.
(55) Mueller, J. E.; Van Duin, A. C.; Goddard, W. A., III Development and validation of ReaxFF reactive force field for hydrocarbon chemistry catalyzed by nickel. *J. Phys. Chem. C* **2010**, *114* (11), 4939−4949.
(56) van Duin, A. C. T.; Baas, J. M.; Van De Graaf, B. Delft molecular mechanics: a new approach to hydrocarbon force fields. Inclusion of a geometry-dependent charge calculation. *J. Chem. Soc., Faraday Trans.* **1994**, *90* (19), 2881−2895.
(57) Zhang, G.; Wang, X.; Yang, F.; Shi, Y.; Song, J.; Lai, X. Energetics and diffusion of hydrogen in hydrogen permeation barrier of α-Al2O3/FeAl with two different interfaces. *Int. J. Hydrogen Energy* **2013**, *38* (18), 7550−7560.
(58) Wu, W.; Lei, X.; Zhong, S.; Sun, B.; Ouyang, C. First-principles insights of hydrogen diffusion dynamics at the α-Al2O3 (0001) surface. *Appl. Surf. Sci.* **2020**, *531*, No. 147263.
(59) Latimer, K.; Dwaraknath, S.; Mathew, K.; Winston, D.; Persson, K. A. Evaluation of thermodynamic equations of state across chemistry and structure in the materials project. *npj Comput. Mater.* **2018**, *4* (1), No. 40.
(60) Jain, A.; Ong, S. P.; Hautier, G.; Chen, W.; Richards, W. D.; Dacek, S.; Cholia, S.; Gunter, D.; Skinner, D.; Ceder, G.; Persson, K. A. Commentary: The Materials Project: A materials genome approach to accelerating materials innovation. *APL Mater.* **2013**, *1* (1), No. 011002.
(61) Guo, F.; Long, C.; Zhang, J.; Zhang, Z.; Liu, C.; Yu, K. Adsorption and dissociation of H2O on Al (1 1 1) surface by density functional theory calculation. *Appl. Surf. Sci.* **2015**, *324*, 584−589.
(62) Hass, K. C.; Schneider, W.; Curioni, A.; Andreoni, W. First-principles molecular dynamics simulations of H2O on α-Al2O3 (0001). *J. Phys. Chem. B* **2000**, *104* (23), 5527−5540.
(63) Lu, Y.-H.; Chen, H.-T. Hydrogen generation by the reaction of H 2 O with Al 2 O 3-based materials: a computational analysis. *Phys. Chem. Chem. Phys.* **2015**, *17* (10), 6834−6843.
(64) Wittbrodt, J. M.; Hase, W.; Schlegel, H. Ab initio study of the interaction of water with cluster models of the aluminum terminated (0001) α-aluminum oxide surface. *J. Phys. Chem. B* **1998**, *102* (34), 6539−6548.
(65) Hass, K. C.; Schneider, W. F.; Curioni, A.; Andreoni, W. The chemistry of water on alumina surfaces: Reaction dynamics from first principles. *Science* **1998**, *282* (5387), 265−268.